Physica C: Superconductivity and its applications 568 (2020) 1353577

Contents lists available at ScienceDirect

Physica C: Superconductivity and its applications

journal homepage: www.elsevier.com/locate/physc

Three-dimensional analysis of the magnetic fields and forces in a coreless HTS linear synchronous motor

Tianyong Gong[a,b], Guangtong Ma[b,*], Ruichen Wang[b], Songlin Li[b], Kang Liu[b], Zhengwei Zhao[b]

[a] Key Laboratory of Magnetic Suspension Technology and Maglev Vehicle, Ministry of Education, Southwest Jiaotong University, Chengdu, China
[b] Applied Superconductivity Laboratory, State Key Laboratory of Traction Power, Southwest Jiaotong University, Chengdu, China

ARTICLE INFO

Keywords:
Linear synchronous motor
Coreless stator
REBCO coil
AC losses
Analytical model

ABSTRACT

High-temperature superconducting (HTS) linear synchronous motor (LSM) with coreless stator presents numerous advantages, among which we stress the high thrust density, large electromagnetic gap as well as the absence of iron losses. This paper aims to investigate the magnetic fields and forces in a coreless HTS LSM and the AC losses in the REBCO coil serving as the excitation system therein. First, a three-dimensional analytical model to calculate the magnetic fields and forces is derived, based on the Biot-Savart law and the Lorenz equations. Secondly, the air-gap magnetic fields and forces are calculated by the analytical model and its effectiveness was confirmed by comparison with the finite element method (FEM) model and experimental measurement. Lastly, the AC losses in the REBCO secondary coil are calculated by a two-dimensional FEM model combined with the three-dimensional analytical model. These results prove that the analytical model presents several advantages of high computational accuracy and less computing-time consumption.

1. Introduction

The coreless high-temperature superconducting (HTS) linear synchronous motor (LSM), due to its high thrust density, large electromagnetic gap and the absence of iron losses, has attracted growing attention in the high-speed transportation systems, such as the high-speed train with wheel-rail support [1,2] and the electrodynamic suspension (EDS) train [3,4]. The EDS train consists of the suspension system and the driving system in which the coreless HTS LSM is used because of its unique advantages, for instance, the robust driving stability and increasing suspension stability with lateral displacements [5]. In order to promote the development of the EDS train and wheel-rail train in the high-speed transportation, a systematical examination of the electromagnetic properties of coreless HTS LSM is essential.

Several studies on the electromagnetic properties of coreless HTS LSM have been carried out in recent years. A 7-kW air-core-type HTS LSM prototype has been designed and installed in a bogie on a 10-m track, and the test results have verified the effectiveness of the coreless HTS LSM for high-speed trains [2]. More recently, the comparison of electromagnetic forces generated by two types of small-scale HTS LSMs with air-core stator and iron-core stator respectively was performed, and it proved that the coreless HTS LSM can provide better thrust and normal force [6]. Besides, based on the Genetic Algorithm method and virtual displacement method, two analytic models were developed in parallel to calculate and optimize the electromagnetic forces of the coreless HTS LSM for the EDS train [5,7]. The obtained results show that the racetrack magnet with elliptical sides can improve thrust and normal force, and the thrust fluctuation can be mitigated by using the optimal parameters of the propulsion coil.

The existing studies on the electromagnetic forces of coreless HTS LSM are mainly based on the experimental measurement and the numerical simulation, where a two-dimensional (2-D) finite element method (FEM) model has been the most common choice. However, the 2-D FEM model cannot take the transverse end effect of LSM into account, leading to the degradation of calculation precision. Therefore, it is necessary to develop a 3-D model for precisely and efficiently evaluating the electromagnetic properties of the coreless HTS LSM. For this purpose, this paper will establish a 3-D analytical model based on the Biot-Savart law and the Lorenz equations to systematically investigate the electromagnetic properties.

2. Analytical model

The coreless HTS LSM consists of the REBCO coil serving as the excitation system and the flat stator made of three-phase copper-based windings embedded in non-magnetic frame, as shown in Fig. 1. The REBCO coil has the racetrack structure composed of two straight sides of length 2l and two semi-circular sides of radius r. The copper windings

* Corresponding author.

https://doi.org/10.1016/j.physc.2019.1353577
Received 25 July 2019; Received in revised form 9 October 2019; Accepted 13 November 2019
Available online 14 November 2019
0921-4534/

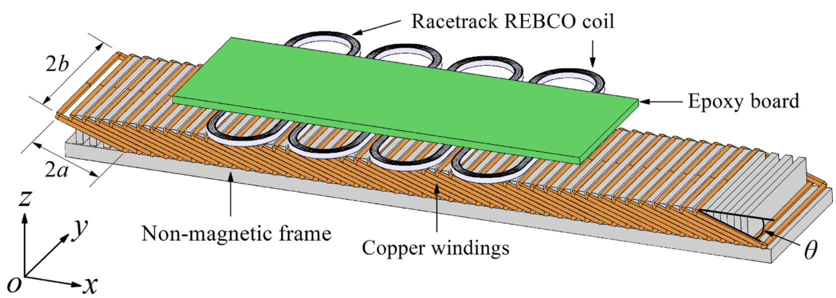

Fig. 1. 3-D analytical model of the coreless HTS LSM with the REBCO coil as the excitation system.

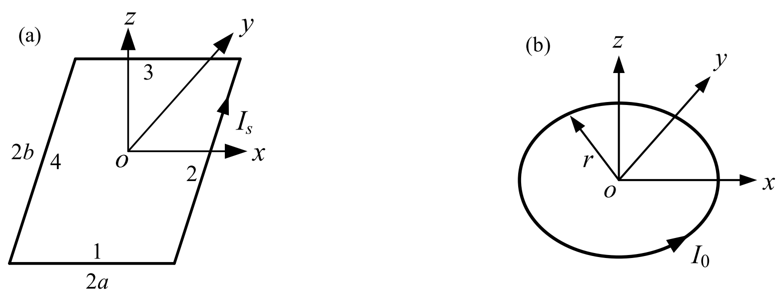

Fig. 2. (a) Rectangular coil and (b) circular coil used to calculate the air-gap magnetic field in coreless HTS LSM.

of the flat stator have the double-layer distributed structure and each copper winding is treated as a rectangular coil. These rectangular coils are clockwise rotated by an angle θ.

Fig. 2 shows a rectangular coil with length 2a and width 2b and a circular coil with radius r, where the rectangular coil carries current I_s and the circular coil carries current I_0. In order to simplify the calculation, none of the cross sections of the coils are considered in the analytical model. The parameters of HTS LSM have been specified in Table 1. and more details can be found in [8,9]. The Cartesian coordinate systems are established at the centers of two coils. The magnetic field components of the rectangular coil and circular coil can be calculated by Biot-Savart law, and then the air-gap magnetic field in coreless HTS LSM can be derived from these field components based on the superposition principle of the magnetic field, due to the absence of magnetic material.

2.1. Magnetic field of rectangular coil

First, the magnetic field components of four finitely long current-carrying conductors marked by numbers 1–4 in Fig. 2(a), can be calculated by (1)–(4) based on the Biot–Savart law [10].

Table 1
Specifications of coreless HTS LSM.

Parameters	Values
REBCO coil	
Width of tape [mm]	4.8
Radius of circular side r [mm]	23
Length of straight side 2l [mm]	170
Width of coil W [mm]	222
Number of coil N	60
Exciting current I_0 [A]	80
Flat stator	
Number of turns N_s	174
Length of rectangular coil 2a [mm]	52.8
Width of rectangular coil 2b [mm]	103
Frequency of stator current f [Hz]	50
Amplitude of stator current I_s [A]	15
LSM	
Pole pitch τ [mm]	60
Electromagnetic gap g [mm]	20

$$[B_{1y}, B_{1z}] = \frac{\mu_0 N_s I_s X_1}{4\pi((y+b)^2 + (z+g)^2)}[-z-g, y+b], \tag{1}$$

$$[B_{2x}, B_{2z}] = \frac{\mu_0 N_s I_s X_2}{4\pi((x-a)^2 + (z+g)^2)}[z+g, -x+a], \tag{2}$$

$$[B_{3y}, B_{3z}] = \frac{\mu_0 N_s I_s X_3}{4\pi((y-b)^2 + (z+g)^2)}[z+g, -y+b], \tag{3}$$

$$[B_{4x}, B_{4z}] = \frac{\mu_0 N_s I_s X_4}{4\pi((x+a)^2 + (z+g)^2)}[-z-g, x+a], \tag{4}$$

where the first and second subscripts of B_{ij} ($i = 1, 2, 3, 4; j = x, y, z$) represent the side number and the component of magnetic field, respectively; μ_0 is the permeability in vacuum; the variables $X_1 - X_4$ are respectively defined as follows,

$$X_1 = \frac{x+a}{\sqrt{(x+a)^2 + (y+b)^2 + (z+g)^2}} - \frac{x-a}{\sqrt{(x-a)^2 + (y+b)^2 + (z+g)^2}}, \tag{5}$$

$$X_2 = \frac{y+b}{\sqrt{(x-a)^2 + (y+b)^2 + (z+g)^2}} - \frac{y-b}{\sqrt{(x-a)^2 + (y-b)^2 + (z+g)^2}}, \tag{6}$$

$$X_3 = \frac{x+a}{\sqrt{(x+a)^2 + (y-b)^2 + (z+g)^2}} - \frac{x-a}{\sqrt{(x-a)^2 + (y-b)^2 + (z+g)^2}}, \tag{7}$$

$$X_4 = \frac{y+b}{\sqrt{(x+a)^2 + (y+b)^2 + (z+g)^2}} - \frac{y-b}{\sqrt{(x+a)^2 + (y-b)^2 + (z+g)^2}}. \tag{8}$$

According to the superposition principle of the magnetic field, the three magnetic field components of one rectangular coil in the x-y plane can be calculated as presented in (9)–(11).

$$B_x = B_{2x} + B_{4x}, \tag{9}$$

$$B_y = B_{1y} + B_{3y}, \tag{10}$$

$$B_z = B_{1z} + B_{2z} + B_{3z} + B_{4z}. \tag{11}$$

Since all rectangular coils in the flat stator are clockwise rotated by an angle θ in the x-z plane (see Fig. 1), the following rotation matrix (12) can be applied.

$$R_y(\theta) = \begin{bmatrix} \cos\theta & 0 & \sin\theta \\ 0 & 1 & 0 \\ -\sin\theta & 0 & \cos\theta \end{bmatrix}. \tag{12}$$

Then, three magnetic field components of the rotated rectangular coil can be expressed by (13).

$$\begin{bmatrix} B_{sx} \\ B_{sy} \\ B_{sz} \end{bmatrix} = R_y(\theta) \begin{bmatrix} B_x \\ B_y \\ B_z \end{bmatrix}. \tag{13}$$

Finally, by using the superposition principle once more, the travelling magnetic field components of the coreless flat stator, including the x-component B_{sx}, y-component B_{sy} and z-component B_{sz} in Cartesian coordinate system, can be obtained through (13) after considering all the rotated rectangular coils and applying the symmetrically three-phase alternating current in these rectangular coils.

2.2. Magnetic field of racetrack coil

The racetrack coil consists of two straight sides and two semi-circular sides (see Fig. 1), where the coordinates of the centers of two semi-circular sides are respectively defined as (0, l, 0) and (0, $-l$, 0). First, the magnetic field components of the two straight sides can be obtained from (2) and (4) when replacing a, b, N_s and I_s with r, l, N and I_0. Secondly, the magnetic field components of the two semi-circular sides are obtained by the following definite integrals [11],

$$B_{cx} = \frac{\mu_0 N I_0 n}{4\pi}\left(\int_0^{\pi} \frac{z\cos\alpha}{r_1^3} + \int_{\pi}^{2\pi} \frac{z\cos\alpha}{r_2^3}\right)d\alpha, \tag{14}$$

$$B_{cy} = \frac{\mu_0 N I_0 m}{4\pi}\left(\int_0^{\pi} \frac{z\sin\alpha}{r_1^3} + \int_{\pi}^{2\pi} \frac{z\sin\alpha}{r_2^3}\right)d\alpha, \tag{15}$$

$$B_{cz} = \frac{\mu_0 N I_0}{4\pi}\left(\int_0^{\pi} \frac{mn - nx\cos\alpha - m(y-l)\sin\alpha}{r_1^3} + \int_{\pi}^{2\pi} \frac{mn - nx\cos\alpha - m(y+l)\sin\alpha}{r_2^3}\right)d\alpha, \tag{16}$$

where the B_{cx}, B_{cy} and B_{cz} represent the x-component, y-component and z-component of the magnetic field, respectively. The r_1 and r_2 are the distances between the field point (x, y, z) and two source points, i.e., (mcosα, l + nsinα, 0) and (mcosα, –l + nsinα, 0) on the two semi-circular sides, respectively.

$$r_1 = \sqrt{x^2 + (y-l)^2 + z^2 + m^2\cos^2\alpha + n^2\sin^2\alpha - 2mx\cos\alpha - 2n(y-l)\sin\alpha}, \tag{17}$$

$$r_2 = \sqrt{x^2 + (y+l)^2 + z^2 + m^2\cos^2\alpha + n^2\sin^2\alpha - 2mx\cos\alpha - 2n(y+l)\sin\alpha}, \tag{18}$$

where m and n represent the major radius and minor radius of an elliptical sides, here $m = n = r$.

The magnetic field components of one racetrack coil, including the x-component B_{rx}, y-component B_{ry} and z-component B_{rz} in Cartesian coordinate system, can be derived from (2), (4), (14)–(16). If the racetrack coil has a transverse displacement Δy, the variable y in (6), (8), (16)–(18) needs to be modified as y – Δy. Finally, the air-gap field of LSM can be quantified by (2), (4), (13)–(16).

2.3. Electromagnetic forces

With the air-gap magnetic field in hand, the Lorenz equations can be applied to calculate the electromagnetic forces of coreless HTS LSM [12],

$$F_x = \sum_i \oint_{\Gamma_i} I_y B_{sz} dl, \tag{19}$$

$$F_y = -\sum_i \oint_{\Gamma_i} I_x B_{sz} dl, \tag{20}$$

$$F_z = \sum_i \oint_{\Gamma_i} (I_x B_{sy} - I_y B_{sx}) dl, \tag{21}$$

where the F_x, F_y and F_z represent the thrust, transverse force and normal force, respectively. The Γ_i represents the center line of the racetrack coil, and the subscript i represents the number of the center line. Here we have assumed $i = 1$. The current vector [I_x, I_y] of racetrack coil is defined by (22) [13].

$$[I_x, I_y] = \begin{cases} \frac{NI_0}{\sqrt{x^2 + (y-l)^2}}[l-y, x](l<y) \\ NI_0[0, sign(x)](-l \le y \le l) \\ \frac{NI_0}{\sqrt{x^2 + (y+l)^2}}[-l-y, x](y<-l) \end{cases}. \tag{22}$$

3. Results and discussions

Based on the aforementioned analytic model, the air-gap magnetic field distribution of the coreless HTS LSM is calculated in the first place and compared with the results of a full 3-D FEM model developed in [8] to verify the analytical model. Secondly, the electromagnetic forces of the HTS LSM under a mover-locked condition are calculated and compared with the results of a 2-D FEM model developed in [9] to further verify the analytical model. Thirdly, the electromagnetic forces under the transverse displacements of the racetrack coil relative to the stator are investigated and the effect that the width of the coreless stator has on forces is studied. Fourthly, the AC losses of the racetrack REBCO secondary coil are evaluated by a 2-D FEM model combined with the 3-D analytical model. By default, only one racetrack coil is considered.

Additionally, we also experimentally verified the 3-D analytical model in terms of the thrust and normal force of a HTS LSM, which will be discussed in Appendix A. In Appendix B, the effect of back iron on the forces of the LSM will be discussed, based on the 3-D analytical model.

3.1. Magnetic field distribution

The horizontal component B_{sx} of the travelling magnetic field generated by the coreless stator is calculated by the proposed 3-D analytical model and the 3-D FEM model developed in [8]. The results evaluated in a rectangular domain of 4τ in the x direction per 4τ in the y direction at 20 mm above the upper surface of the stator (z direction), are shown in Fig. 3. The two models show a good agreement on the distribution of magnetic field, which serves as a validation for the 3-D analytical model. It can also be seen from Fig. 3 that the magnetic field presents a significantly non-uniform distribution along the width of the coreless stator, and it decreases from the symmetric cross section ($y = 0$) to the transverse end of stator.

Fig. 4 shows the horizontal component B_{rx} and vertical component B_{rz} of the magnetic field at a height of 20 mm generated by the racetrack coil under different exciting currents, where the solid lines represent the results of the 3-D analytical model and the open symbols represent those of the 3-D FEM model. The inset shows the line where the magnetic field is extracted. The analytical and numerical results

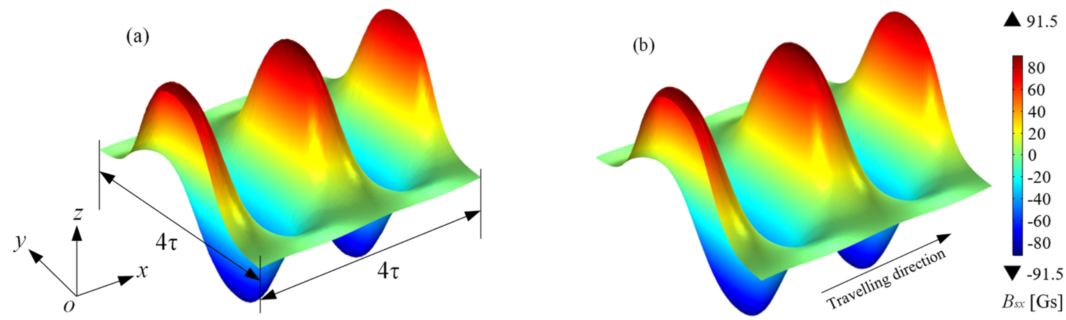

Fig. 3. Horizontal component B_{sx} of travelling magnetic field generated by the coreless stator, which is calculated by the 3-D analytical model (a) and the 3-D FEM model (b) developed in [8], respectively.

agree well on the distribution of the magnetic field, which is independent of the location and the exciting current of the coil. From Figs. 3 and 4, we can conclude that the 3-D analytical model can reproduce accurately the air-gap magnetic field. Since the 3-D analytical model only needs to solve the definite integrals (14)–(16), its computing-time consumption is much less than the 3-D FEM model.

3.2. Electromagnetic forces

Fig. 5 shows the thrust F_x and normal force F_z of the coreless HTS LSM under different amplitudes of the stator current when the electromagnetic gap remains 20 mm, where the solid lines represent the results of the 3-D analytical model and the open symbols represent those of a 2-D FEM model [9]. Only a slight difference can be found on the electromagnetic forces between the two models. Furthermore, the thrust and normal force behave as sinusoids and they increase linearly with the amplitude of the stator current.

Fig. 6(a) shows the amplitudes of thrust and normal force with respect to the width of stator 2b. It is found that the two forces first increase linearly with the width of the stator, and then increase slowly when the width of the stator is around the width of racetrack coil. Lastly the two forces remain constant after the width of stator becomes larger than the width of the racetrack coil. It is noteworthy that the maximum value of the normal force is larger than that of thrust. The explanation is as follows: the transverse travelling magnetic field component B_{sy} under different gap heights above the upper surface of the stator is shown in Fig. 6(b), and the inset on the top left corner of the figure shows the normal force generated by the two circular sides of the racetrack coil. Fig. 6(b) portrays that the transverse magnetic field is mainly distributed at the edges of the stator. Since the two circular sides are located near the transverse end of the stator, an additional normal force will be generated from the electromagnetic interaction between the circular sides and the transverse magnetic field according to (21). However, the transverse magnetic field makes no difference to the thrust. That is the main reason why the normal force is larger than the thrust. Furthermore, the amplitude of the additional normal force will increase with the decrease of electromagnetic gap, as shown in the inset.

Besides, when the gap is below 8 mm, the amplitude of the normal force declines after reaching its maximum value, which results from the end effect of the stator. That is to say, when the width of racetrack coil is equal to the width of the stator, the circular sides of the racetrack coil suffer from the maximum transverse component shown in Fig. 6(b), thus the additional normal force reaches its maximum value. With the increase of the width of the stator, the circular sides suffer from a smaller transverse magnetic field, so the amplitude of the additional normal force decreases, leading to a decline of normal force. In addition, the amplitude of thrust has a slight increment after the width of stator exceeds the width of racetrack coil, since the thrust generated by the straight sides of the racetrack coil always increases with the increase of the width of the stator. That can be explained by the nonuniform distribution of the travelling magnetic field along the width of stator, as shown in Fig. 3. According to the above discussion, we can conclude that the maximum forces happen when the racetrack coil and coreless stator keeps the same width, which is independent of the gap. Therefore, the optimal width of the racetrack coil is the width of the coreless stator.

A 2-D FEM model is the most common choice to calculate the electromagnetic forces of a LSM, but it ignores the transverse end effect of the LSM and brings the decrease of calculation precision. Therefore, several actions need to be taken to improve its precision. Fig. 7(a) shows the effective width of the racetrack coil for calculating the

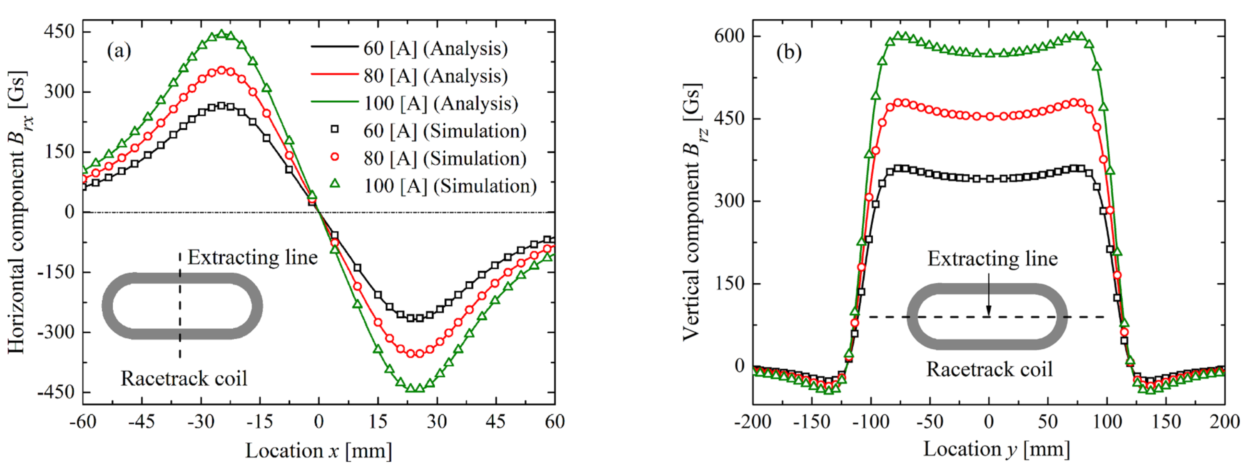

Fig. 4. Horizontal component B_{rx} (a) and vertical component B_{rz} (b) of the magnetic field at a height of 20 mm generated by the racetrack coil under different exciting currents, where the solid lines represent the results of the 3-D analytical model and the open symbols represent the results of the 3-D FEM model.

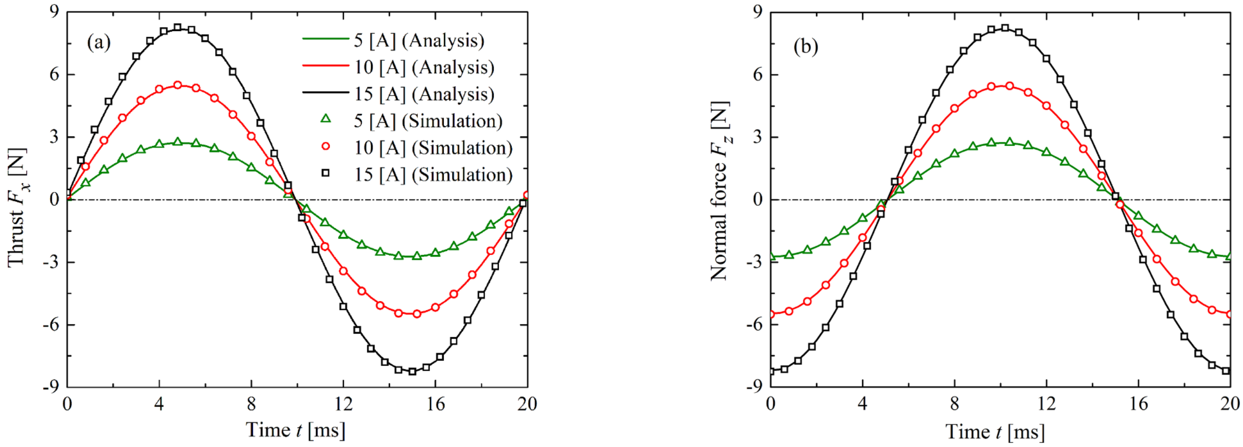

Fig. 5. Thrust F_x (a) and normal force F_z (b) of the coreless HTS LSM under different amplitudes of stator current, where the solid lines represent the results of the 3-D analytical model and the open symbols represent those of a 2-D FEM model [9].

electromagnetic forces of coreless LSM based on the 2-D FEM model [9]. The average effective width in Fig. 7(a) is obtained by averaging the effective widths of both the thrust and normal force. Two cases can be discerned, when the width of the racetrack coil is larger than that of the stator, the effective width is about 0.97 times the width of the stator. On the other hand, when the width of the stator is larger than the racetrack coil, the effective width is now 0.91 times the width of the racetrack coil. In both cases, one can find that the average effective width is closer to the smaller one between both the stator and racetrack coil. It is due to the transverse end effect of the smaller coil that the effective width is a little smaller than the width of this one. If the effective width of racetrack coil is not defined, one could select the smaller width between the racetrack coil and stator. That is to say, the smaller one of two widths of racetrack coil and stator can be selected to calculate the forces of a coreless LSM by resorting to a 2-D FEM model. It needs to be clarified that the results of 2-D FEM model shown in Fig. 5 were calculated using the width of the stator, so the forces are a little larger than the one of the 3-D analytical model.

Fig. 7(b) shows the amplitudes of the electromagnetic forces (open symbols) calculated by the 2-D FEM model after considering the average effective width. In order to facilitate the understanding of the comparison, the forces calculated by the 3-D analytical model are shown again herein. Which shows a good agreement on the amplitudes of forces between the 2-D FEM model and the 3-D analytical model. There is a relatively large divergence only near the transition region where the widths of both stator and racetrack coil are the same. It can be concluded that a 2-D FEM model can give approximate results when calculating the electromagnetic forces of a coreless LSM by considering the effective width of racetrack coil, but the divergence still exists since the transverse end effect cannot be completely characterized by an effective width.

Fig. 8 shows the amplitudes of thrust, normal force and transverse force with respect to the plus y-direction transverse displacement Δy ($\Delta y > 0$) of the racetrack coil when $2b = W$. It can be found that the amplitudes of thrust and normal force slowly decrease before one circular side of racetrack coil moves out the upper surface of stator, i.e., $\Delta y < r$, that is mainly because of the fact that the thrust and normal force generated by the circular side decrease. Likewise, when $\Delta y > r$, the thrust and normal force linearly decrease, since the two forces generated by the straight sides decrease. On the contrary, the transverse force linearly increases when $\Delta y < r$, and then slowly increases to a saturated value. It is worth mentioning that the transverse force trends to improve the transverse stability of the LSM, because the direction of transverse force is opposite to the direction of displacement.

3.3. AC losses of racetrack REBCO secondary coil

Based on the developed 3-D analytical model and the 2-D FEM model [9], the AC losses of racetrack REBCO secondary coil can be obtained. Recently, various numerical methods have been developed to calculate the AC losses of REBCO coil, such as the H-formulation [13–16], T-A formulation [17–19] and the integral equations method

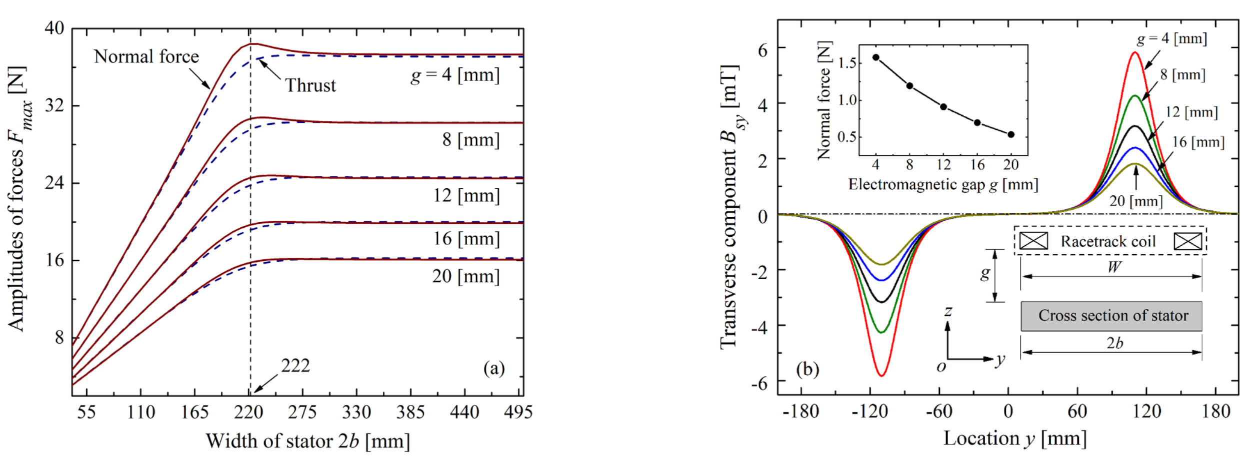

Fig. 6. Amplitudes of thrust and normal force with respect to the width of stator 2b (a) and the transverse travelling magnetic field component B_{sy} (b) under different gap heights above the upper surface of the stator. The inset shows the normal force generated by the two circular sides of the racetrack coil.

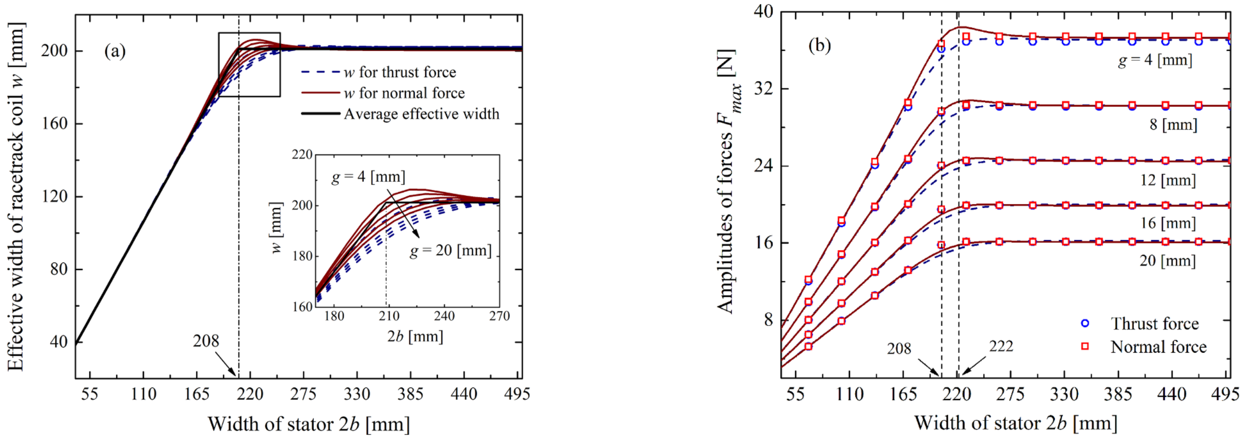

Fig. 7. (a) Effective width of racetrack coil for calculating the electromagnetic forces of coreless LSM by a 2-D FEM model, where the average effective width is obtained by averaging the effective widths of both the thrust and normal force. (b) Maximum electromagnetic forces (open symbols) calculated by the 2-D FEM model after considering the average effective width.

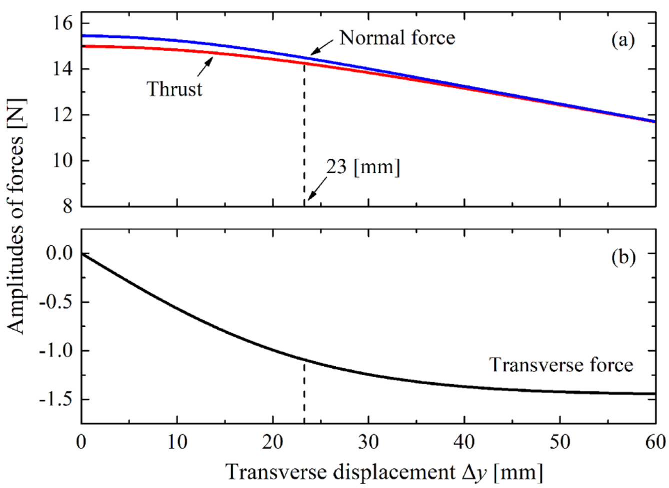

Fig. 8. Amplitudes of thrust, normal force (a) and transverse force (b) with respect to the transverse displacement of racetrack coil.

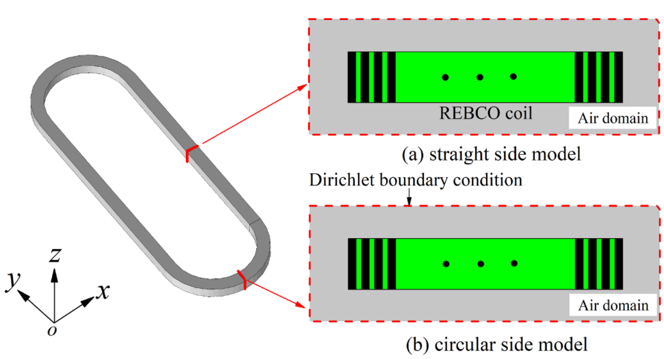

Fig. 9. 2-D FEM model of the racetrack REBCO secondary coil, where the magnetic field on the Dirichlet boundary condition is calculated by the 3-D analytical model.

[20,21]. In this paper, the widely accepted homogenous H-formulation has been adopted and a 2-D FEM model is developed to calculate the AC losses of the racetrack REBCO secondary coil. For the purpose of considering the transverse end effect of the LSM, the cross sections of both the straight side and circular side of REBCO coil are selected and the corresponding models are named straight side model and circular side model respectively, as shown in Fig. 9, where the magnetic field on the Dirichlet boundary condition is calculated by the 3-D analytical model.

To verify the developed 2-D FEM model, the AC losses of racetrack REBCO coil presented in [13] are calculated by the 2-D FEM model and a comparison of the results is shown in Fig. 10(a). The slight difference on the AC losses between the developed model and the full 3-D FEM models [13] validates the 2-D model. It is a fact that the 2-D FEM model coupled with the 3-D analytical model costs less computing time than the full 3-D FEM model. For instance, in order to calculate one data point in Fig. 10(a) the 2-D FEM model costs about 0.17 h and the 3-D FEM model costs about 17.6 h on a PC (Intel i7-7700, 3.60 GHz, RAM 32 GB). Fig. 10(b) shows the AC losses of the straight side and the circular side of the REBCO coil. One can find that the AC losses of the straight side are a little larger than that of the circular side, due to the longer effective length of the straight side [13]. After the exciting current reaches 120 A, however, the AC losses of the circular side quickly increase and then exceed those of the straight side owing to the effect of self-field of racetrack coil. The inset shows the instantaneous AC losses for the case of an exciting current of 100 A, it can be seen that the maximum value of the instantaneous losses of the straight side is a little lager than those of the circular side.

According to the validated 2-D FEM model, the AC losses of the racetrack REBCO coil, serving as the excitation system of the LSM, are calculated under the mover-locked condition and the results for different amplitudes and frequencies of the stator current are shown in Fig. 11. Since the amplitude of the induced transport current in the REBCO secondary coil is dependent of not only the frequency and amplitude of the stator current [8], but also the resistance and capacitance of REBCO secondary coil [22], the induced current is difficult to be determined in the FEM model. Here, we assumed that the induced current is proportional to the amplitude of the stator current, and that a stator current of 20 A corresponds to the induced current of 20 A. An additional supplement is that the frequency of the induced transport current is the same with the frequency of stator current [6]. The magnitude of travelling magnetic field on the Dirichlet boundary condition was shown in Fig. 3. Before applying the travelling magnetic field to the boundary, a decay of 0.5 s has been taken into account for the flux creep and relaxation of the magnetic field in REBCO coil, which follows the starting process of a HTS LSM [23].

It can be inferred from Fig. 11 that the AC losses of REBCO secondary coil increase nonlinearly in the logarithmic coordinate system with the normalized exciting current for all given amplitudes of the stator current, which is different with the characteristic presented in Fig. 10. The main reason for the difference on the nonlinear variation law of the losses could be that the REBCO secondary coil carried a hybrid exciting current composed of the enforced direct current and the

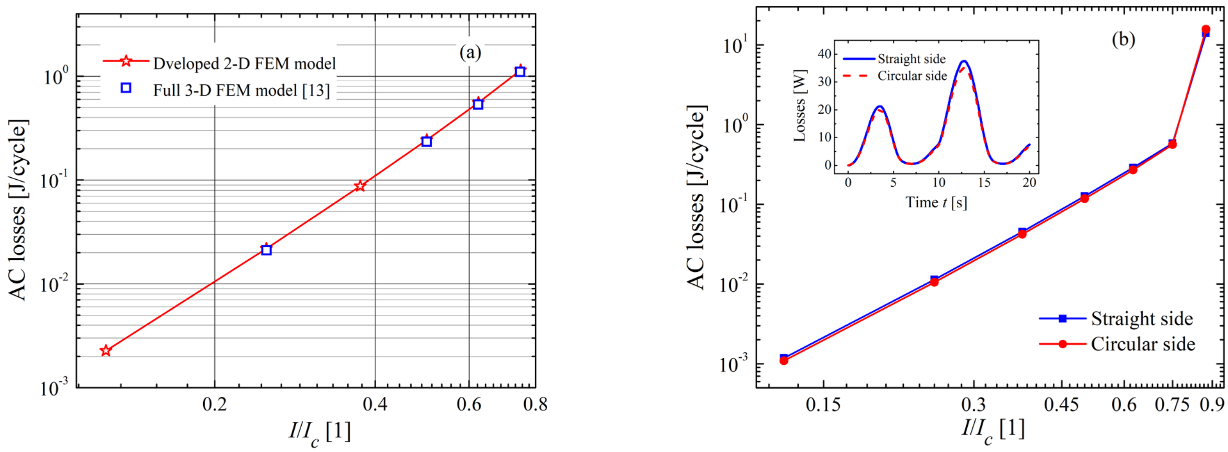

Fig. 10. (a) AC losses of REBCO coil calculated respectively by the developed 2-D FEM model and the full 3-D FEM model [13] and (b) a comparison of the AC losses of the straight side and circular side.

induced alternating current. It is easy to understand that an increase of the amplitude of the stator current resulted in the rise of the losses. Fig. 11(b) shows the AC losses of REBCO secondary coil with respect to the normalized exciting current for varying frequencies of the stator current. When the exciting current of the coil is below 50 A, the losses are almost independent of the frequency of the stator current, which may be because the AC losses are dominated by the hysteresis losses. After the exciting current of the coil exceeds 50 A, there is a large region occupied by the overcritical current density in the REBCO secondary coil, leading to a considerably large increase of the losses. As seen from the two insets in Fig. 11, the average power losses augment with the increase of the amplitude and frequency of the stator current.

4. Conclusions

Based on the Biot-Savart law and the Lorenz equations, a general 3-D analytical model for calculating the electromagnetic properties of a coreless HTS LSM was established and confirmed. With the help of the 3-D analytical model, a 2-D FEM model was developed to evaluate the AC losses of the racetrack REBCO coil serving as the excitation system of the LSM. An extended application of the developed 3-D analytical model was given in the Appendix. The following conclusions are drawn.

The exhibited 3-D analytical model is capable of precisely reproducing the air-gap magnetic field and electromagnetic forces in a coreless HTS LSM. Compared to both the full 2-D FEM and 3-D FEM models, the 3-D analytical model costs much less computing time and is therefore more promising for the design optimization of a coreless HTS LSM.

The maximum thrust and normal force happen when the widths of both the racetrack coil and the coreless stator are the same, which is independent of the gap. The circular side of racetrack coil will increase the normal force more than the thrust because of the transverse travelling magnetic field component, which cannot be considered in a 2-D FEM model. By considering the effective width of racetrack coil, a 2-D FEM model can approximately calculate the electromagnetic forces of a coreless LSM. If the effective width of the racetrack coil is not defined, the smaller one of two widths of the racetrack coil and the stator can be selected to calculate the forces by resorting to a 2-D FEM model.

By resorting to the 2-D FEM model combined with the 3-D analytical model, the AC losses of the racetrack REBCO coil serving as the excitation system of the coreless LSM are obtained. The results show that the developed 2-D FEM model can reproduce precisely and efficiently the AC losses of REBCO secondary coil subjected to the travelling magnetic field.

Declaration of Competing Interest

The authors declare that they have no known competing financial interests or personal relationships that could have appeared to influence the work reported in this paper.

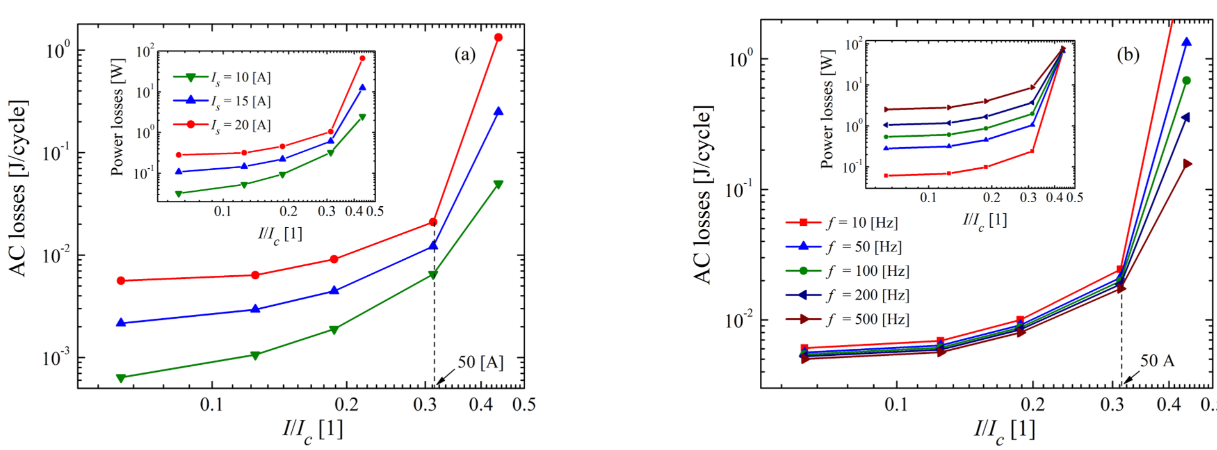

Fig. 11. AC losses of the racetrack REBCO secondary coil under different amplitudes (a) and frequencies (b) of the stator current.

Acknowledgments

The authors would like to acknowledge Dr. Loïc Quéval for providing technical comments on the analytical model and Manuel Perez for his help reading this manuscript and for providing valuable comments.

This work was supported by the National Natural Science Foundation of China under Grants 51722706 and 51707164.

Appendix A. Validation of the 3-D analytical model

To experimentally validate the exhibited 3-D analytical model, the electromagnetic forces obtained from the 3-D analytical model were compared with the results of the experimental measurement, which has been presented in our previous work [6]. Fig. A1 shows the comparison of the electromagnetic forces between the experimental measurement and the 3-D analytical model under different amplitudes of stator current. The electromagnetic gap remains 25 mm and the frequency of stator current is 30 Hz. The solid lines represent the 3-D analytical results and the open symbols represent the measured results. Due to the absence of iron core, the zero-order components of the thrust F_x and normal force F_z have been eliminated during the data processing. Fig. A1 illustrates that the 3-D analytical model reproduces the measured results, regardless of the amplitudes of stator current. The forces of the experimental measurement exhibited a significant variation as a result of the induced current in the REBCO coil subjected to travelling magnetic field [6,8]. Nonetheless, the fundamental components of both the thrust and normal force follow proportional relation with the stator current, because the amplitude of travelling magnetic field is proportional with the stator current.

Based on the Fast Fourier Transform, the fundamental components of the thrust and normal force in Fig. A1 are extracted and shown in Fig. A2, where the results of the 2-D FEM model of the coreless HTS LSM have also been shown to better verify the 3-D analytical model. A good agreement can be found on the fundamental components of the thrust and normal force between the experimental measurement and 3-D analytical model, and the maximum relative error is less than 7%, thus validating the 3-D analytical model. As expected, the amplitudes of the fundamental components of the thrust and normal force, obtained from both the 2-D FEM model and 3-D analytical model, increase linearly with the amplitude of stator current.

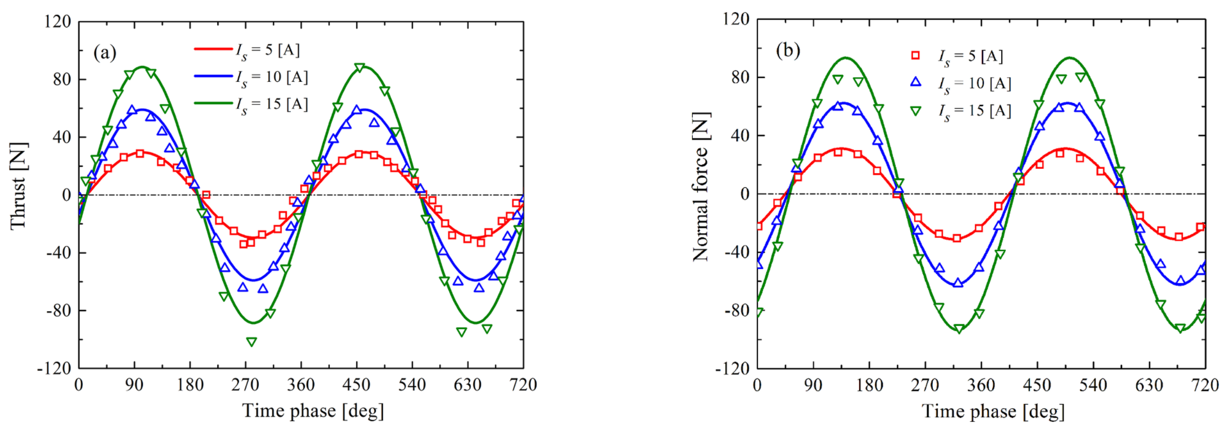

Fig. A1. Comparison of the electromagnetic forces of a coreless HTS LSM between the experimental measurement [6] and the 3-D analytical model, (a) thrust and (b) normal force under different amplitudes of stator current, where the solid lines represent the 3-D analytical results and the open symbols represent the measured results.

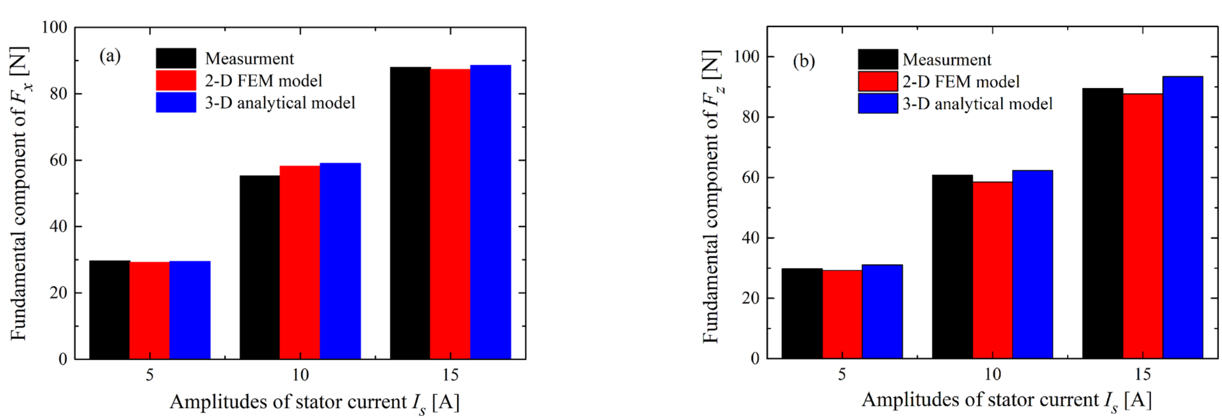

Fig. A2. Fundamental components of the thrust F_x (a) and normal force F_z (b) under different amplitudes of stator current.

Appendix B. Introduction of back iron

The developed analytical model can be used to calculate the air-gap magnetic field and electromagnetic forces of HTS LSM with the back iron in the flat stator and racetrack coil. As expected, the introduction of back iron into the LSM can lead to an increase in thrust and normal force [24,25]. Fig. B1(a) shows the vertical component B_{rz} of magnetic field generated by the racetrack coil in the center point shown in the inset, where the open symbol represents the result of a full 3-D FEM model and the solid line represents those of the 3-D analytical model. It is found that the analytical model can reproduce precisely the result of FEM model when the magneto motive force of coil is below 5 kA·turns, but the error of analytical model

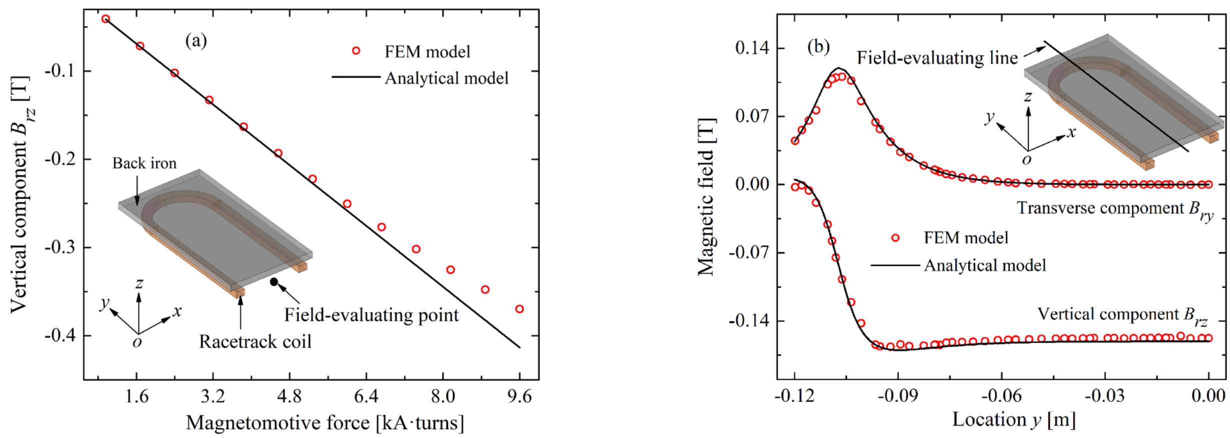

Fig. B1. (a) Vertical component B_{rz} of magnetic field generated by the racetrack coil in the center point and (b) the transverse component B_{ry} and vertical component B_{rz} of magnetic field in the center line of the coil with a magneto motive force of 4.8 kA·turns.

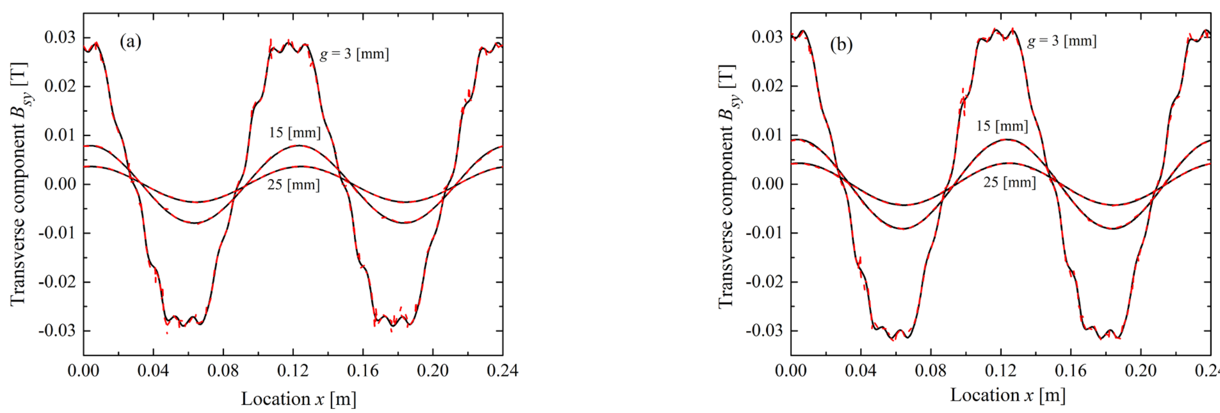

Fig. B2. Transverse component B_{sy} of the travelling magnetic field at the transverse end of the stator without back iron (a) and with back iron (b).

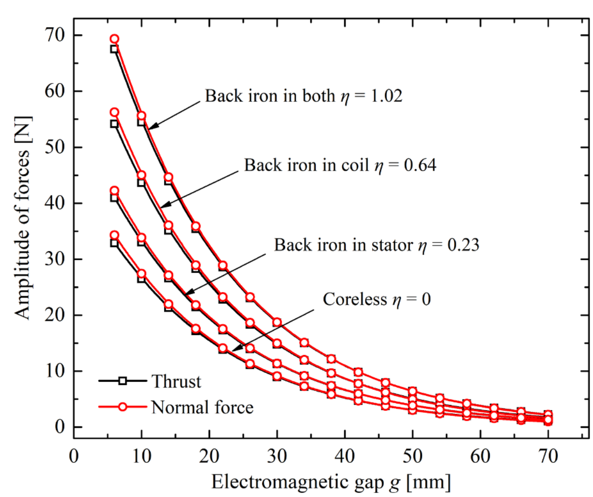

Fig. B3. Amplitudes of the thrust and normal force as a function of electromagnetic gap of the LSM with and without back iron.

occurs and augments after the magneto motive force exceeds 5 kA·turns on account of the saturation of back iron, which is not able to be represented in the analytical model. Fig. B1(b) shows the transverse component B_{ry} and vertical component B_{rz} of magnetic field generated by the racetrack coil in the center line shown in the inset with a magneto motive force of 4.8 kA·turns. These identical results of the two models prove that the analytical model can reproduce precisely the magnetic field of racetrack coil with a back iron when unsaturated.

Fig. B2 shows the transverse component B_{sy} of travelling magnetic field at the transverse end of the stator under different gap heights, i.e., 3 mm, 15 mm and 25 mm. The magnetic field of the stator without back iron is shown in Fig. B2(a) and the magnetic field of the stator with back iron is shown in Fig. B2(b), where the dashed lines represent the results of a 3-D FEM model and the solid lines represent those of the 3-D analytical model. The identical results validate the analytical model. It is important to point out that the back iron in stator is difficult to be saturated because of the small value of travelling magnetic field [5]. Besides, by comparison with Fig. B2(a) and (b), one can observe that the magnetic field of the stator with back iron is a little larger than that of the stator without back iron. When the gap exceeds 15 mm, the waveform of magnetic field becomes very smooth, which implies a significantly less harmonic component for the large-gap HTS LSM.

The amplitudes of the thrust and normal force as a function of electromagnetic gap of the LSM with and without back iron are shown in Fig. B3. In which, the enhanced coefficient η of the forces is defined as follows,

$$\eta = \frac{F_{ironcore} - F_{aircore}}{F_{aircore}}, \tag{A1}$$

where $F_{iron\ core}$ represents the force of the LSM with back iron, and $F_{air\ core}$ represents the one without back iron.

It can be inferred from Fig. B3 that the thrust and normal force with back iron in both the coil and stator are twice larger than the one without back iron, and the enhanced coefficient of back iron in coil is larger than the one in stator. In particular, the sum of the enhanced coefficients of both the coil and stator respectively with back iron is less than the one simultaneously in both because of the electromagnetic interaction between the two back irons.

References

[1] C.Y. Lee, J.H. Lee, J.M. Jo, C.B. Park, W.H. Ryu, Y.D. Chung, Y.J. Hwang, T.K. Ko, S.Y. Oh, J. Lee, Conceptual design of superconducting linear synchronous motor for 600-kph wheel-type railway, IEEE Trans. Appl. Supercond. 24 (3) (2014) 3600304.

[2] C.B. Park, C.Y. Lee, S. Yoon, S. Kim, Development of a small-scale superconducting LSM using Gd-Ba-Cu-O high-temperature superconducting wire, IEEE Trans. Energy Convers 31 (4) (2016) 1250–1256.

[3] H.W. Lee, K.C. Kim, L. Ju, Review of maglev train technologies, IEEE Trans. Magn. 42 (7) (2006) 1917–1925.

[4] K. Kuwano, M. Igarashi, S. Kusada, K. Nemoto, T. Okutomi, S. Hirano, T. Tominaga, M. Terai, T. Kuriyama, K. Tasaki, T. Tosaka, K. Marukawa, S. Hanai, T. Yamashita, Y. Yanase, H. Nakao, M. Yamaji, The running tests of the superconducting maglev using the HTS magnet, IEEE Trans. Appl. Supercond. 17 (2) (2007) 2125–2128.

[5] T.Y. Gong, G.T. Ma, Y. Cai, H.Y. Qian, J. Li, Y.K. Deng, Z.M. Zhao, Calculation and optimization of propulsion force of a real-scale REBCO magnet for EDS train, IEEE Trans. Appl. Supercond. 29 (5) (2019) 3602606.

[6] K. Liu, Z.W. Zhao, T.Y. Gong, Y. Cai, C. Wang, P.B. Zhou, W. Xu, G.T. Ma, The reduced fluctuation in the electromagnetic forces of a coreless HTS linear synchronous motor, Physica C557(2019)49–54.

[7] Z.W. Zhao, K. Liu, C. Wang, W.H. Zhang, J. Li, L. Han, X.L. Song, G.T. Ma, The establishment of an analytical model for coreless HTS linear synchronous motor with a generalized racetrack coil as the secondary, IEEE Trans. Appl. Supercond. 29 (5) (2019) 5203105.

[8] G.T. Ma, T.Y. Gong, H. Zhang, Z.T. Wang, X.T. Li, C. Yang, K. Liu, W.H. Zhang, Experiment and simulation of REBCO conductor coils for an HTS linear synchronous motor, IEEE Trans. Appl. Supercond. 27 (4) (2017) 5201805.

[9] T.Y. Gong, G.T. Ma, H.Y. Qian, K. Liu, C. Wang, Z.W. Zhao, W.H. Zhang, Electromagnetic investigation of a high temperature superconducting linear synchronous motor for high-speed railway, IEEE Trans. Appl. Supercond. 28 (3) (2018) 5202305.

[10] W.G.V. Rosser, The Biot-Savart law, Phys. Educ.9(1974)493.

[11] H.W. Zhao, S. Crozier, An inverse design method for elliptical MRI magnets, Meas. Sci. Technol. 12 (5) (2001) 566–574.

[12] G.T. Ma, Considerations on the finite-element simulation of high-temperature superconductors for magnetic levitation purposes, IEEE Trans. Appl. Supercond. 23 (5) (2013) 3601609.

[13] V.M.R. Zermeño, F. Grilli, 3D modeling and simulation of 2 G HTS stacks and coils, Supercond. Sci.Technol. 27 (4) (2014) 044025.

[14] Z. Hong, W. Yuan, M. Ainslie, Y. Yan, R. Pei, T.A. Coombs, AC losses of superconducting racetrack coil in various magnetic conditions, IEEE Trans. Appl. Supercond. 21 (3) (2011) 2466–2469.

[15] V.M.R. Zermeño, A.B. Abrahamsen, N. Mijatovic, B.B. Jensen, M.P. Sørensen, Calculation of alternating current losses in stacks and coils made of second generation high temperature superconducting tapes for large scale applications, J. Appl. Phys. 114 (17) (2013) 173901.

[16] L. Queval, V.M.R. Zermeno, F. Grilli, Numerical models for AC loss calculation in large-scale applications of HTS coated conductors, Supercond. Sci. Technol. 29 (2) (2016) 024007.

[17] H.M. Zhang, M. Zhang, W.J. Yuan, An efficient 3D finite element method model based on the T-A formulation for superconducting coated conductors, Supercond. Sci. Technol. 30 (2) (2017) 024005.

[18] F. Liang, S. Venuturumilli, H.M. Zhang, M. Zhang, J. Kvitkovic, S. Pamidi, Y.W. Wang, W.J. Yuan, A finite element model for simulating second generation high temperature superconducting coils/stacks with large number of turns, J. Appl. Phys. 122 (4) (2017) 043903.

[19] E. Berrospe-Juarez, V.M.R. Zermeno, F. Trillaud, F. Grilli, Real-time simulation of large-scale HTS systems: multi-scale and homogeneous models using the T-A formulation, Supercond. Sci. Technol. 32 (6) (2019) 065003.

[20] R. Brambilla, F. Grilli, L. Martini, F. Sirois, Integral equations for the current density in thin conductors and their solution by the finite-element method, Supercond. Sci. Technol. 21 (10) (2008) 105008.

[21] F.G.R Martins, F. Sass, R. de Andrade, Simulations of REBCO tape jointless double crossed loop coils with an integral equations method, Supercond. Sci. Technol. 32 (4) (2019) 044002.

[22] F. Yen, X. Chen, R.B. Wang, J.M. Zhu, J. Li, G.T. Ma, Induced currents in close-ended type-ii superconducting coils, IEEE Trans. Appl. Supercond. 23 (6) (2013) 8202005.

[23] T.Y. Gong, G.T. Ma, C. Wang, Z.T. Wang, Numerical simulation of the thermo-electromagnetic properties of superconducting magnet in travelling magnetic field, in: proceedings of the 20th international conference on electrical machines and systems (ICEMS), 2017, pp. 1–5.

[24] F. Yen, J. Li, S.J. Zheng, L. Liu, G.T. Ma, J.S. Wang, S.Y. Wang, W. Liu, A single-sided linear synchronous motor with a high temperature superconducting coil as the excitation system, Supercond. Sci. Technol. 23 (10) (2010) 105015.

[25] J. Li, F. Yen, S. Zheng, S. Wang, J. Wang, Normal force analysis on a high temperature superconducting linear synchronous motor, IEEE Trans. Appl. Supercond. 22 (3) (2012) 5200304.